

Warped Bayesian Linear Regression for Normative Modelling of Big Data

Charlotte J. Fraza^{a,b}, Richard Dinga^a, Christian F. Beckmann^{a,b,d}, Andre F. Marquand^{a,b,c}

^a*Donders Centre for Cognitive Neuroimaging, Donders Institute for Brain, Cognition and Behaviour, Radboud University, Nijmegen, the Netherlands*

^b*Department of Cognitive Neuroscience, Radboud University Medical Centre, Nijmegen, the Netherlands*

^c*Department of Neuroimaging, Centre for Neuroimaging Sciences, Institute of Psychiatry, King's College London, London, UK*

^d*Oxford Centre for Functional Magnetic Resonance Imaging of the Brain (FMRIB), University of Oxford, Oxford, UK*

Abstract

Normative modelling is becoming more popular in neuroimaging due to its ability to make predictions of deviation from a normal trajectory at the level of individual participants. It allows the user to model the distribution of several neuroimaging modalities, giving an estimation for the mean and centiles of variation. With the increase in the availability of big data in neuroimaging, there is a need to scale normative modelling to big data sets. However, the scaling of normative models has come with several challenges.

So far, most normative modelling approaches used Gaussian process regression, and although suitable for smaller datasets (up to a few thousand participants) it does not scale well to the large cohorts currently available and being acquired. Furthermore, most neuroimaging modelling methods that are available assume the predictive distribution to be Gaussian in shape. However, deviations from Gaussianity can be frequently found, which may lead to incorrect inferences, particularly in the outer centiles of the distribution. In normative modelling, we use the centiles to give an estimation of the deviation of a particular participant from the ‘normal’ trend. Therefore, especially in normative modelling, the correct estimation of the outer centiles is of utmost importance, which is also where data are sparsest.

Here, we present a novel framework based on Bayesian Linear Regression with likelihood warping that allows us to address these problems, that is,

to scale normative modelling elegantly to big data cohorts and to correctly model non-Gaussian predictive distributions. In addition, this method provides also likelihood-based statistics, which are useful for model selection.

To evaluate this framework, we use a range of neuroimaging-derived measures from the UK Biobank study, including image-derived phenotypes (IDPs) and whole-brain voxel-wise measures derived from diffusion tensor imaging. We show good computational scaling and improved accuracy of the warped BLR for certain IDPs and voxels if there was a deviation from normality of these parameters in their residuals.

The present results indicate the advantage of a warped BLR in terms of; computational scalability and the flexibility to incorporate non-linearity and non-Gaussianity of the data, giving a wider range of neuroimaging datasets that can be correctly modelled.

Keywords: Machine learning, UK Biobank, Big Data, Bayesian Linear Regression, Normative Modelling

1 Introduction

Big data has become more widely available in neuroimaging (UK Biobank, ENIGMA, ABCD study, PNC, among others) [1], [2], [3], [4]. This has ignited a renewed interest in modelling normal brain development, to estimate quantitative brain-behaviour mappings and capture deviations from such models to derive neurobiological markers of different psychiatric disorders. These neurobiological markers could move us closer towards individualized and precision medicine [5]. Until now, the neurobiological markers for psychiatric disorders have been mostly developed with studies that used classifiers trained in a case-control setting. Counter-intuitively, an increase in sample size has shown to reduce the accuracy of classifying cases from controls for psychiatric disorders [6]. One of the main reasons for this decrease in accuracy has been posed to be the heterogeneity in the participants both biologically and behaviorally, which can only fully be captured by a large data set [6]. Normative modelling is an emerging method used to understand this heterogeneity in the population. Similar to growth charts in pediatric medicine, which describe the distribution of height or weight of children according to their age and sex, normative models can be used to model the distribution of neuroimaging derived phenotypes in a population, including the mean and centiles of variation [7], according to age, gender, or other demographic or

21 clinical variables [8]. The deviations from this normative range can be quan-
22 tified statistically, for example as Z-scores, which have been linked to several
23 psychiatric disorders [7], [9], [10], [11], [12], [13].

24 Although promising, there are still certain challenges in performing nor-
25 mative modelling on big neuroimaging data. First of all, Normative models
26 have been mainly developed using Gaussian process regression. [14]. Gaus-
27 sian process regression is flexible and accurate, but a drawback is its com-
28 putational complexity, which is governed by the need to compute the exact
29 inverse of the covariance matrix. This inversion scales poorly with an in-
30 crease in data points [15]. Therefore, using these models on large datasets
31 requires extensive computational power and is often not feasible (typically
32 beyond a few thousand subjects). Furthermore, most normative models as-
33 sume the modelled distribution is Gaussian. However, distributions diverging
34 from Gaussianity are frequently found in specific neuroimaging modalities.
35 These non-Gaussian signals cannot be accounted for using a standard nor-
36 mative model based on Gaussian process regression. We argue that mod-
37 elling non-Gaussianity is important in general and is frequently overlooked
38 by the neuroimaging community in that most regression methods used in
39 practice –often implicitly– assume Gaussian residuals. Thus, there is a need
40 to develop methods that can flexibly handle the computational demand and
41 non-Gaussianity of big data sets.

42 In this paper, we propose a next-generation framework based on Bayesian
43 linear regression (BLR) to address these challenges. We introduce an exten-
44 sion of the BLR method for accurately modelling non-Gaussian distributions
45 using a likelihood warping technique, giving a warped BLR model. The new
46 framework has several benefits over previously used methods: (i) A BLR
47 model can use a linear combination of non-linear basis functions (such as B-
48 splines) which can be considered to provide a low-rank approximation of the
49 Gaussian process regression models [16]. However, the BLR model has con-
50 siderably better computational scaling, since the complexity of the model is
51 fixed according to a set of basis-functions. Therefore, the model can be scaled
52 much more easily to large datasets. Furthermore, a set of model coefficients
53 can be estimated that can easily be shared without the need to share the data
54 (e.g. to compute a cross-covariance matrix for new data points), thus mak-
55 ing it easier to make predictions on new datasets. (ii) The non-Gaussianity
56 of the residuals can be modelled by the flexible warping of the Gaussian
57 function, which gives more options to model different types of neuroimaging
58 data that cannot be accurately modelled using a standard BLR. (iii) Efficient

59 model selection criteria are naturally defined for the warped BLR through
60 the marginal likelihood and can be calculated in closed form. The marginal
61 likelihood gives a balance between model complexity and model fit. This can
62 aid in choosing the optimal model for a specified imaging modality.

63 We will demonstrate this model by testing it on different types of neu-
64 roimaging data derived from the UK Biobank dataset. The UK Biobank
65 dataset has several magnetic resonance imaging (MRI) imaging modalities,
66 including structural and functional brain data. With over 40,000 partici-
67 pants' MRI data from 40 to 80 years old, this provides a rich set of differ-
68 ent neuroimaging data and defines a benchmark for future population-based
69 studies. In this work, we will present the warping function and recommend
70 how to use it for several data modalities. First, we give an illustrative exam-
71 ple using image-derived phenotypes (IDPs), which are convenient and widely
72 used summary measures of brain function and structure [17]. Specifically, we
73 will show a detailed example of estimating a normative model for white mat-
74 ter hyperintensities (WMHs). WMHs have been shown before to demonstrate
75 quite non-Gaussian behaviour [18], and are therefore a good example where
76 the warped BLR could be preferred over the B-spline BLR. Second, we show
77 the scalability of this method by performing a whole-brain analysis for cer-
78 tain diffusion tensor imaging (DTI) measures. We use DTI measurements,
79 as there are large associations with age and we expect certain non-linear and
80 non-Gaussian trends in the data [19].

81 Finally, we want to evaluate the link between brain imaging abnormality
82 scores and behaviour. Therefore, deviations from normal brain functioning
83 are associated with cognitive functioning. The deviations are captured by
84 Z-scores, which are shown to correlate with measures of intelligence in the
85 UK Biobank dataset, such as; numerical memory, reaction time and visual
86 memory.

87 In summary, the main contributions of the paper are to give: (i) a new
88 comprehensive framework for big data normative modelling; (ii) the intro-
89 duction of the novel methodological approach for modelling non-Gaussian
90 response variables; (iii) an extensive and didactic evaluation of this frame-
91 work on the UK Biobank cohort and (iv) a demonstration of the 'Predictive
92 Clinical Neuroscience software toolkit' (PCNtoolkit) for big data normative
93 modelling. Ultimately, we hope this paper will give deeper insight into the
94 application of normative models on different types of neuroimaging modal-
95 ities.

96 2. Materials and methods

97 2.1. Sample

98 All the data used came from the UK Biobank imaging dataset [1]. Full
99 details on the design of the study and the preprocessing steps can be found
100 in subsequent papers [17], [20]. Briefly, the data used contains around 10,000
101 participants of the 2017 release and additional longitudinal data of around
102 5,000 subjects of the 2020 release. The participants were between 40 and 80
103 years of age, with around 47 % males.

104 In this study, two types of analyses were performed using different datasets.
105 For the first analysis, a dataset containing IDPs was used. For consistency
106 with existing work, the IDPs were processed using FUNPACK [21], which
107 is an automatic normalisation, parsing and cleaning kit, developed at the
108 Wellcome Centre for Integrative Neuroimaging. The IDPs include three
109 main imaging modalities: structural, functional and diffusion brain imag-
110 ing. Among these IDPs, there are very gross measures, such as the total
111 amount of brain volume, to more detailed measurements, such as the con-
112 nectivity between two brain regions. In total 819 neuroimaging IDPs were
113 used for subsequent analysis, see B.1 for the list of IDPs used. Furthermore,
114 we also tested our model on another set of IDPs; 150 FreeSurfer measures,
115 which were preprocessed with FreeSurfer v6.1.0, using a T_2 -weighted image
116 where available, see B.1 for the list of the FreeSurfer measures used.

117 For the second analysis, a whole-brain model was built, using voxel-wise
118 fractional anisotropy (FA) and mean diffusivity (MD) measures. The data
119 were processed using the UKB pipelines; including the DTI fitting tool DTI-
120 FIT and a tract-based spatial statistics (TBSS) style analysis, which gave us
121 the skeletonised DTI files. In total, around 10,000 participants with dMRI-
122 scans passed the quality control applied by the UK Biobank [17]. Afterwards,
123 we added two extra exclusion criteria. First, participants were removed if
124 their Z-score of the discrepancy between the dMRI image and the struc-
125 tural T1 image was higher than three, based on data-field 25731 in the UK
126 Biobank. Second, participants were removed if their Z-score of the number
127 of outlier slices was higher than three, which is a reflection of the movement
128 of the participant during the scan, based on data-filed 25746-2.0 in the UK
129 Biobank. For the covariates we used age, gender and dummy coded site
130 variables.

131 *2.2. Cognitive data*

132 We used the cognitive phenotypes that were extracted from the UK
133 biobank using FUNPACK [21] to evaluate the cognitive associations with
134 the deviations from the normative model. These measures are derived from
135 the 13 cognitive tests present in the UK Biobank, see the UKB showcase. The
136 tests were administered using a touchscreen questionnaire and included nu-
137 merical memory, reaction time, fluid intelligence, visual memory and prospec-
138 tive memory. Later other tests that measured executive function, declarative
139 memory and non-verbal reasoning were added [22]. For full details on the
140 different cognitive tests applied in UK Biobank see [23]. An overview of all
141 the measures used in this study is presented in the supplementary E.6.

142 *2.3. Normative model formulation*

143 We use a flexible normative modelling framework to model different types
144 of neuroimaging data. We have N subjects with brain data $\{\mathbf{y}_n\}_{n=1}^N$, each of
145 dimension D (e.g. the number of voxels or IDPs) and acquired from one of
146 S different scanning sites. We use \mathbf{Y} to denote an $N \times D$ matrix containing
147 these variables, where y_{nd} denotes the n -th subject and d -th neuroimaging
148 variable. Since the neuroimaging variables are estimated separately here,
149 we simplify the notation by using \mathbf{y} to denote the vector of observations
150 from a single variable and y_n for a single observation. In general, we want
151 to predict the distribution of the value for each voxel or brain region, the
152 dependent variable (\mathbf{y}), from a set of covariates $\{\mathbf{x}_n\}_{n=1}^N$ (e.g. age, gender or
153 site), the independent variables. In this paper, we adopt a straightforward
154 approach to model nonlinear relationships, by applying a basis expansion to
155 the independent variables. A common approach is to use polynomials, but
156 these can be a poor choice, as they can induce global curvature [24]. Here
157 we apply a common B-spline basis expansion (specifically, cubic splines with
158 5 evenly spaced knot points), although other approaches are also possible.
159 We denote this expansion by $\phi(\mathbf{x})$, with Φ an $N \times K$ matrix containing the
160 basis expansion for all subjects. In the applied model, y is assumed to be the
161 result of a linear combination of the B-spline basis function transformation
162 plus a noise term:

$$y = \mathbf{w}^T \phi(\mathbf{x}) + \epsilon_s \quad (1)$$

163 With \mathbf{w} the estimated vector of weights and $\epsilon_s = \mathcal{N}(0, \beta_s^{-1})$ a Gaussian noise
164 distribution for site s , with mean zero and a noise precision term β_s (i.e. the
165 inverse variance). All the noise precision terms from the different sites will

166 be combined in a vector $\boldsymbol{\beta}$ and the site precision matrix $\boldsymbol{\Lambda}_{\boldsymbol{\beta}}$, which has $\boldsymbol{\beta}$
167 along the leading diagonal and is the inverse of the site covariance matrix
168 $\boldsymbol{\Lambda}_{\boldsymbol{\beta}} = \boldsymbol{\Sigma}_{\boldsymbol{\beta}}^{-1}$. Note that we allow the noise precision to vary across sites in
169 order to accommodate inter-site variation along with site-specific intercepts
170 (i.e. dummy coded site regressors in the design matrix). We have shown
171 previously that this approach provides an efficient way to accommodate site
172 effects in normative modelling [25].

173 Following similar derivations as given by Huertas et al. [16], we consider
174 a BLR model, placing a Gaussian prior over our model parameters $p(\mathbf{w}|\boldsymbol{\alpha}) =$
175 $\mathcal{N}(\mathbf{w}|0, \boldsymbol{\Lambda}_{\boldsymbol{\alpha}}^{-1})$, with $\boldsymbol{\alpha}$ the hyper-parameters that the weights depend on. The
176 Gaussian prior is assumed to have a mean zero and a precision matrix $\boldsymbol{\Lambda}_{\boldsymbol{\alpha}}$,
177 with the precision matrix the inverse of the covariance matrix $\boldsymbol{\Sigma}_{\boldsymbol{\alpha}} = \boldsymbol{\Lambda}_{\boldsymbol{\alpha}}^{-1}$.
178 As shown in Huertas et al. [16], $\boldsymbol{\Lambda}_{\boldsymbol{\alpha}}$ can be quite general, but here we use a
179 simple isotropic precision matrix $\boldsymbol{\Lambda}_{\boldsymbol{\alpha}} = \alpha \mathbf{I}$. The Gaussian prior choice allows
180 us to compute the posterior distribution of \mathbf{w} in a closed form:

$$p(\mathbf{w}|\mathbf{y}, \boldsymbol{\Phi}, \boldsymbol{\alpha}, \boldsymbol{\beta}) = \frac{\text{likelihood} \times \text{prior}}{\text{marginal likelihood}} = \frac{\prod_n p(y_n|\boldsymbol{\Phi}, \boldsymbol{\beta}, \mathbf{w})p(\mathbf{w}|\boldsymbol{\alpha})}{p(\mathbf{y}|\boldsymbol{\Phi}, \boldsymbol{\alpha}, \boldsymbol{\beta})} \quad (2)$$

181 The posterior for each subject can then be found using the standard
182 derivations of the posterior [26]:

$$\begin{aligned} p(\mathbf{w}|\mathbf{y}, \boldsymbol{\Phi}, \boldsymbol{\alpha}, \boldsymbol{\beta}) &= \mathcal{N}(\mathbf{w}|\bar{\mathbf{w}}, \mathbf{A}^{-1}) \\ \mathbf{A} &= \boldsymbol{\Phi}^T \boldsymbol{\Lambda}_{\boldsymbol{\beta}} \boldsymbol{\Phi} + \boldsymbol{\Lambda}_{\boldsymbol{\alpha}} \\ \bar{\mathbf{w}} &= \mathbf{A}^{-1} \boldsymbol{\Phi}^T \boldsymbol{\Lambda}_{\boldsymbol{\beta}} \mathbf{y} \end{aligned} \quad (3)$$

183 We use a Type II maximum likelihood approach (i.e. empirical Bayes),
184 optimizing the denominator of the posterior to find the optimal hyper-parameters
185 $\boldsymbol{\alpha}$ and $\boldsymbol{\beta}$. This gives an automatic trade-off between model fit and model com-
186 plexity. The marginal likelihood is maximized by minimizing the negative
187 log likelihood (NLL):

$$\begin{aligned}
 \text{NLL} &= -\log(p(\mathbf{y}|\boldsymbol{\alpha}, \boldsymbol{\beta})) \\
 &= -\log\left(\int p(\mathbf{y}|\mathbf{w}, \boldsymbol{\beta})p(\mathbf{w}|\boldsymbol{\alpha})d\mathbf{w}\right) \\
 &= -\left(\frac{N}{2}\log|\boldsymbol{\Lambda}_\beta| - \frac{ND}{2}\log 2\pi - \frac{N}{2}\log|\boldsymbol{\Lambda}_\alpha| - \frac{N}{2}\log|\mathbf{A}|\right. \\
 &\quad \left. - \frac{1}{2}\sum_{n=1}^N (\mathbf{y} - \Phi\bar{\mathbf{w}})^T \boldsymbol{\Lambda}_\beta (\mathbf{y} - \Phi\bar{\mathbf{w}}) - \bar{\mathbf{w}}^T \boldsymbol{\Lambda}_\alpha \bar{\mathbf{w}}\right) \quad (4)
 \end{aligned}$$

The optimal hyper-parameters $\boldsymbol{\alpha}$ and $\boldsymbol{\beta}$ are often estimated using a conjugate gradient optimisation of the NLL, where the derivatives can be computed directly. However, here we used Powell’s method to fit the hyper-parameters. Powell’s method is a derivative-free method, which in this case is faster, because computing the derivatives of the marginal likelihood with respect to the hyper-parameters is computationally very expensive. Finally, the predictive distribution is given by:

$$\hat{y} = \mathcal{N}(\bar{\mathbf{w}}^T \phi(\mathbf{x}), \phi(\mathbf{x})^T \mathbf{A}^{-1} \phi(\mathbf{x}) + \beta_s^{-1}) \quad (5)$$

188 *2.3.1. Likelihood warping*

189 In order to model non-Gaussian error distributions, we employed a ‘warped’
 190 likelihood [27]. This involves applying a non-linear monotonic warping func-
 191 tion φ_i to the input data during the model fit, with the index i indicating a
 192 different warping function (e.g. SinArcsinh, Box-Cox etc.). This is similar
 193 to the classical statistical technique of variable transformation, but has the
 194 advantage that the parameters of the transformation are optimised during
 195 model fitting, to provide the optimal mapping that ensures that model resid-
 196 uals have a Gaussian form. The warped functions are chosen such that they
 197 have a closed form inverse and are differentiable, which has several bene-
 198 fits: first, non-Gaussian data can be mapped (i.e. warped) exactly to better
 199 match Gaussian modelling assumptions or the predictions can be warped
 200 back to the original non-Gaussian space; second, it allows inference, predic-
 201 tion and computation of error measures all in closed form; finally, we can
 202 construct compositions of functions from the invertible monotonic warping
 203 functions that can greatly improve the expressivity of the model in transform-
 204 ing non-Gaussian distributed data \mathbf{y} to a Gaussian form, \mathbf{z} , where inference
 205 is straightforward [28]. This is done by applying a compositional warping
 206 function φ to the observations \mathbf{y} :

$$\begin{aligned}\varphi(\cdot) &= \varphi_i(\varphi_{i-1}(\dots(\varphi_2(\varphi_1(\cdot))))\dots) \\ \mathbf{z} &= \varphi(\mathbf{y}; \boldsymbol{\gamma})\end{aligned}\tag{6}$$

207 With $\boldsymbol{\gamma}$ denoting the hyper-parameter(s) of different warping functions.
 208 The warping transformation allows us to compute error measures in the
 209 warped space and to describe the deviations of subjects under a Gaussian
 210 error distribution in the form of pseudo Z statistics, even if the original data
 211 distribution is non-Gaussian.

212 The optimal hyper-parameters ($\boldsymbol{\alpha}$, $\boldsymbol{\beta}$ and $\boldsymbol{\gamma}$) are calculated by minimizing
 213 the warped NLL. The warped NLL can be found by accounting for the change
 214 of variables in the probability density function [28]:

$$p_{\mathbf{y}}(\mathbf{y}) = p_{\mathbf{z}}(\varphi(\mathbf{y})) |\nabla \varphi(\mathbf{y})|$$

215 With $\nabla \varphi(\cdot)$ the Jacobian of the transformation, which is diagonal and
 216 therefore we can simplify as a product of the individual terms:

$$p_{\mathbf{y}}(\mathbf{y}) = p_{\mathbf{z}}(\varphi(\mathbf{y})) \prod_{i=1}^n \frac{d\varphi(y_n)}{dy}$$

217 If we take the negative log of this equation the warped NLL will remain
 218 the same as equation 4, except for replacing the \mathbf{y} by the transformed $\varphi(\mathbf{y})$
 219 and the inclusion of the Jacobian term that takes the change of volume
 220 induced by the warping into account, thereby ensuring a valid probability
 221 measure, for details see [28]:

$$\begin{aligned}\text{Warped NLL} &= -\log(p(\mathbf{y}|\boldsymbol{\alpha}, \boldsymbol{\beta}, \boldsymbol{\gamma})) \\ &= \text{NLL} - \sum_{n=1}^N \log \frac{d\varphi(y_n)}{dy}\end{aligned}\tag{7}$$

222 2.3.2. Computational complexity

223 The optimization of the hyper-parameters is controlled by the minimiza-
 224 tion of the warped NLL. The warped NLL consists of the basic BLR NLL

225 term and the log-derivatives of the warping φ_i functions, which are known
226 in closed-form by construction. The complexity of the warped BLR model
227 is then roughly the same as the classic BLR. However, the warped NLL is
228 optimized for an extra hyper-parameter $\boldsymbol{\gamma}$, which could lead to the presence
229 of more local minima, making the optimization process slightly slower [28].

230 2.3.3. Warped composition function

231 Different elementary functions can be used to create the warped compo-
232 sition function φ . For this paper, we test affine, Box-Cox and SinhArcsinh
233 transformations and compositions of these transformations:

$$\begin{aligned}\varphi_{Affine}(\mathbf{y}; \boldsymbol{\gamma}) &= a + b\mathbf{y} \\ \varphi_{Box-Cox}(\mathbf{y}; \boldsymbol{\gamma}) &= \frac{\text{sgn}(\mathbf{y})|\mathbf{y}|^\lambda - 1}{\lambda} \\ \varphi_{SinhArcsinh}(\mathbf{y}; \boldsymbol{\gamma}) &= \sinh(b * \text{arcsinh}(\mathbf{y}) - a)\end{aligned}\quad (8)$$

With $\boldsymbol{\gamma}$ the respective parameters of the different warping functions. For the SinhArcsinh warping we also applied a reparametrization [29], as this empirically gave more stable results:

$$\begin{aligned}\varphi_{SinhArcsinh}(\mathbf{y}; \boldsymbol{\gamma}) &= \sinh(b * \text{arcsinh}(\mathbf{y}) + \epsilon * b) \\ a &= -\epsilon * b\end{aligned}$$

234 2.4. Model selection

We evaluate the models using different model selection criteria. First, we calculate the explained variance (EV) of the model. It is expected that the gain in fit for the warped BLR will be highly dependent on the flexibility of the model. Therefore, the Bayesian Information Criterion (BIC) is also considered:

$$BIC = k * \log(N) + 2 * NLL$$

235 Which penalises for model complexity. Here N denotes the number of partic-
236 ipants in the training set, NLL the negative log-likelihood. k is the number of
237 free parameters. Note that we use the marginalized form of the NLL, which
238 already takes into account the number of estimated coefficients. Therefore,
239 the BIC only needs to be corrected for the added complexity of the degrees

240 of freedom of the model (i.e. the parameters that are not integrated out).
241 For the standard BLR this is two, one for the precision over the weights and
242 one for the precision over the noise (α and β respectively). For the warped
243 SinArcsinh BLR two extra degrees of freedom are added for the shape param-
244 eters (a and b). The BIC gives a good trade-off between the extra flexibility
245 found in the warped BLR model and the better fit of the model. Finally, the
246 mean standardized log-likelihood (MSLL) is used as a third model criterion.
247 The MSLL takes into account the mean error and the estimated prediction
248 variance.

249 2.5. Deviance scores and correlation to cognitive phenotypes

We want to find a statistical estimate of how much each participant de-
viates from the normal range. This is done by computing a Z-score for each
subject n , also denoting explicitly the dependence on each voxel or IDP d :

$$z_{nd} = \frac{y_{nd} - \hat{y}_{nd}}{\sqrt{\sigma_d^2 + (\sigma_*^2)_d}} \quad (9)$$

250 With, \hat{y}_{nd} the predicted mean and y_{nd} the true response. Normalized
251 by $\sigma_d^2 = (\beta_s^{-1})_d$ the estimated noise variance (i.e. reflecting variation in
252 the data) and $(\sigma_*^2)_d = \phi(\mathbf{x})^T \mathbf{A}_d^{-1} \phi(\mathbf{x})$ the variance attributable to modelling
253 uncertainty for the d -th voxel. For the warped statistic, we compute the
254 Z-scores in the warped (i.e. Gaussian) space. The true response variables
255 are warped to the Gaussian space to ensure the underlying assumption of
256 normality is satisfied by the construction of the warping functions.

257 Afterwards, to ensure our model can also be applied for behavioural and
258 clinical estimations, we look at the correlations between the Z-scores from
259 the IDPs and the whole brain analysis, and the cognitive scores of the UK
260 Biobank. For the IDPs, we directly correlate the Z-scores and the cognitive
261 phenotypes through a Spearman correlation. For the whole-brain analysis,
262 we first make a summary statistic of the Z-scores by calculating the extreme
263 value distribution. We model the extreme value distribution by looking at
264 the mean of the top 1% of the deviations across the whole brain [10]. The
265 extreme value statistics give the largest deviations per subject from the nor-
266 mal pattern, which have shown to be strongly correlated to behaviour [10],
267 [30]. Afterwards, we apply a principal component analysis (PCA) on the
268 cognitive phenotypes to give a one-factor solution. This first component has
269 been shown to be correlated to the ‘general’ factor of cognitive ability or the

270 ‘g-factor’ [31]. Lastly, we compute the Spearman coefficient between the first
271 principal component and the summary deviation score.

272 **3. Results**

273 *3.1. Performance of the warped Bayesian linear regression model for IDPs*

274 All the statistical analyses were performed in Python version 3.8, using
275 the PCNtoolkit. The BLR algorithm from the PCNtoolkit was chosen for
276 all experiments. We considered age, binary gender and binary site ID within
277 the covariance matrix. We used a standard BLR or we transformed the
278 age covariate with a B-spline of order three with three knots. The Powell
279 method was selected for the optimizer. We randomly split the dataset into
280 50% training and 50% test and reported all the error metrics on the test
281 set. In the PCNtoolbox, several warpings can be chosen depending on the
282 imaging modality one wants to model. We tested several warping functions
283 (affine, Box-Cox and SinhArcsinh) and compositions of these warping func-
284 tions. Preliminary testing showed that the SinhArcsinh warping gave the
285 best fit compared to the alternatives evaluated. Therefore, in this paper,
286 only the results of the SinhArcsinh warping are presented.

287 In figure 1, Bland-Altman plots are shown comparing the standard BLR
288 and the B-spline BLR. The figure presents different model selection criteria:
289 MSLL and BIC (EV can be seen in supplement figure A.8). The plots demon-
290 strate that for most IDPs a non-linear B-spline BLR model performs better
291 than a standard BLR. Indicating that non-linearity is a key component that
292 should be accounted for in modelling neuroimaging data.

293 In figure 2, Bland-Altman plots are shown that compare the B-spline
294 BLR and the warped BLR models for all IDPs, using the MSLL and BIC
295 (EV can be seen in supplement figure A.8). We also plotted the difference
296 in absolute values of the skewness and kurtosis. In figure 3, the same plots
297 are shown for the FreeSurfer measures. We included them separately, as
298 they were preprocessed separately (i.e. we did not use the IDPs provided
299 by UK Biobank and instead ran the Freesurfer reconstructions manually).
300 The plots show that for specific IDPs the warped BLR performs better than
301 the B-spline BLR. When we examined these IDPs more closely, it was noted
302 that they demonstrated distinct non-Gaussian behaviour. An example of
303 such behaviour is given down below with the WMHs (white matter hyper-
304 intensities). In the supplementary table C.3, we provide a summary of some
305 of the results for different IDPs that can help inform which neuroimaging

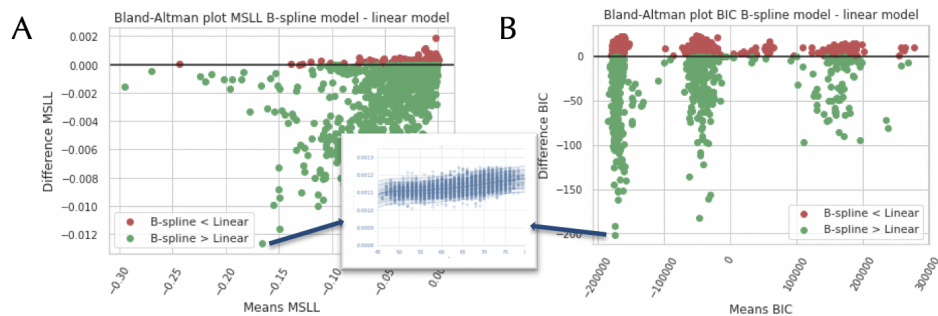


Figure 1: Bland-Altman plots comparing the standard and B-spline Bayesian Linear Regression (BLR) models, using Image-Derived Phenotypes (IDPs). Each dot indicates one IDP. The models are compared according to the following model selection criteria: the Mean Standardized Log Loss (MSLL) (A) and the Bayesian Information Criteria (BIC) (B). The green colour indicates a better fit for the non-linear B-spline model compared to the linear model. We also plotted a zoomed-in view of the model fit for one of the IDs.

306 modalities are best modelled with the warped BLR. For an indication of the
307 effect sizes of the model selection criteria for the different model settings,
308 see supplementary tables D.4 and D.5. Note also that the MSLL and EV
309 do not clearly reflect differences in the shape of the predictive distribution.
310 For example, for the IDs, there is no average difference between the warped
311 and non-warped model (Fig. 2 panel A and supp. fig. A.8 panel B), yet
312 the warped model consistently yields a predictive distribution –and resultant
313 Z-score distribution– that is less (or equivalently) skewed and kurtotic (Fig.
314 2 panels C and D).

315 In figure 4 and 5, we show the results of an illustrative analysis predicting
316 WMH load across ageing to demonstrate how the performance of the warped
317 BLR model compares to a B-spline BLR. The figures show the B-spline BLR
318 and warped BLR results for WMHs at one-time point and the longitudinal
319 data of two-time points. The results demonstrate that (i) the non-linearity
320 of the data is sufficiently captured with a B-spline transformed BLR (ii)
321 the WMHs show a distinctly non-Gaussian variance pattern, which is better
322 predicted by the warped BLR. Thus, indicating that if the data has a non-
323 Gaussian distribution for the residuals a warped BLR is preferred over a
324 B-spline BLR.

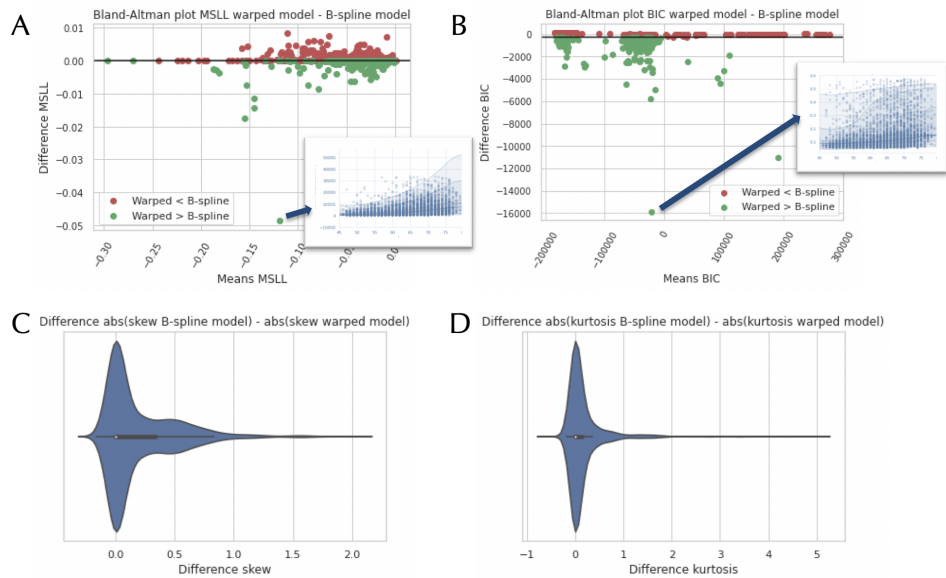


Figure 2: Bland-Altman plots comparing the B-spline and warped Bayesian Linear Regression (BLR) models, using Image-Derived Phenotypes (IDPs). The models are compared according to the following model selection criteria: the Mean Standardized Log Loss (MSLL) (A) and the Bayesian Information Criteria (BIC) (B). The green colour indicates a better fit for the warped model compared to the B-spline model. We also plotted a zoomed-in view of the model fit for two of the IDPs. On images C and D, we show the difference in absolute values of the skewness and kurtosis between the B-spline and warped model. A more positive value indicates that the B-spline model had a higher skewness or kurtosis than the warped model.

3.1.1. Correlation deviance scores WMHs and cognitive phenotypes

We also wanted to correlate the warped BLR model output of the WMHs to behavioural variables to ensure that the model can be used for behavioural predictions. We loaded all cognitive phenotypes available in UK Biobank according to the FUNPACK categorization, including: reaction time, numeric memory, prospective memory etc. (for a full list of the cognitive phenotypes used, see the supplementary table E.6). We calculated the deviance Z-scores according to formula 9. Afterwards, we calculated the Spearman correlation between the cognitive phenotypes and the Z-scores. Numeric memory (ID: 4259, 'Digits entered correctly') was modestly but significantly correlated with the warped Z-scores: $\rho = -0.0331$, $p = 0.0262$. In other words, if a participant's WMH deviation from normal development increases the number of

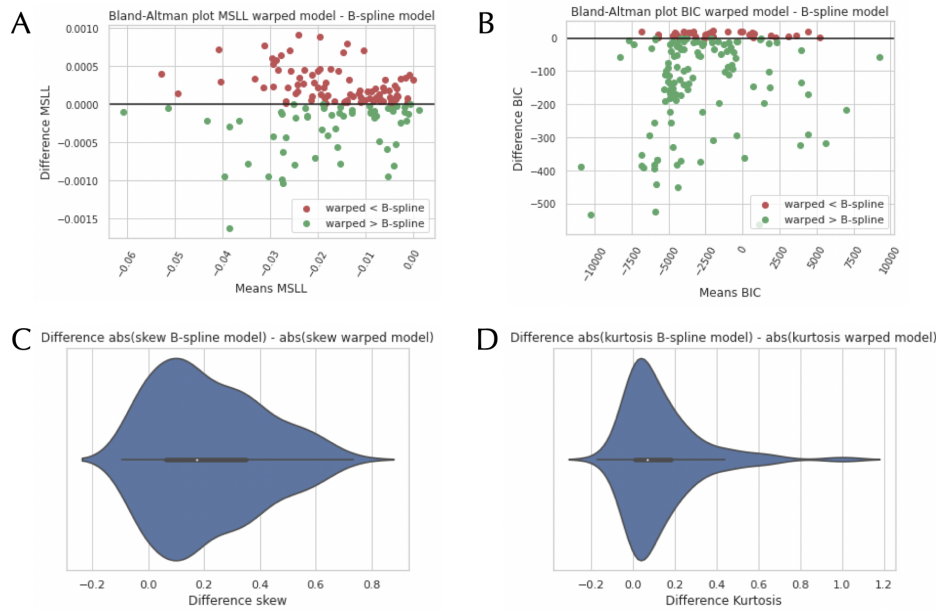


Figure 3: Bland-Altman plots comparing the B-spline and warped Bayesian Linear Regression (BLR) models, using the FreeSurfer measurements. The models are compared according to the following model selection criteria: the Mean Standardized Log Loss (MSSL) (A) and the Bayesian Information Criteria (BIC) (B). We also plotted a zoomed-in view of the model fit for one of the IDPs. On images C and D, we show the difference in absolute values of the skewness and kurtosis between the B-spline and warped model. A more positive number means a better fit for the warped model compared to the B-spline model.

337 correctly remembered digits drops.

338 Lastly, to illustrate the value of normative models in a longitudinal con-
339 text, we tested for an association between change in WMHs and change in
340 cognitive phenotypes of the longitudinal data to see if WMH load is corre-
341 lated to cognitive decline. We performed a statistical Wilcoxon rank-sum
342 test on the participants' cognitive phenotypes contrasting subjects that have
343 a difference in the Z-scores > 0.5 , which corresponds to a difference in half
344 a standard deviation, versus the participants that do not. Intuitively, this
345 contrasts individuals who are following an expected trajectory of ageing with
346 those who deviate from such a trajectory. Highly significant associations were
347 found with the reaction time (ID: 404, 'Duration to first press of snap-button
348 in each round') $W = 5.5641$, $p < 0.001$ and with the Trail Making Test (ID:

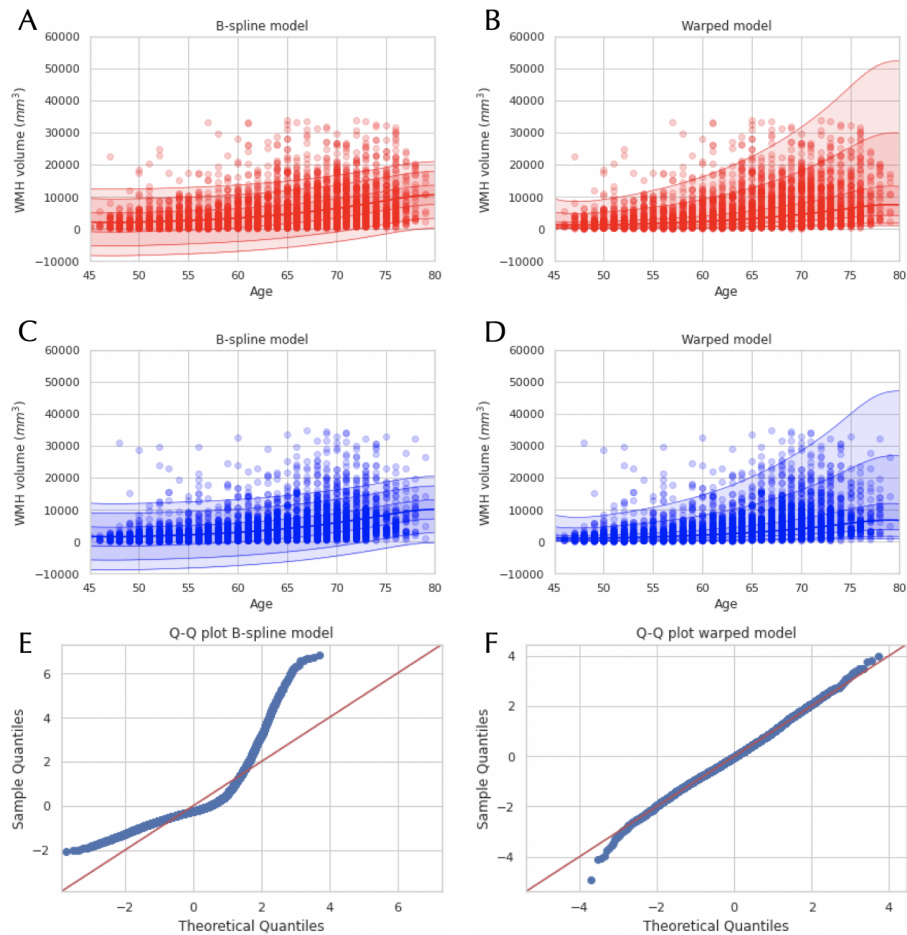


Figure 4: White matter hyperintensities (WMHs) modelled as a function of age using a Bayesian Linear Regression (BLR) model. Images A and C demonstrate the model fit using a regular Gaussian B-spline BLR, for the female and male cohorts respectively, both visualizing the mean prediction and the centiles of variation for the WMHs. Images B and D show comparable fits for a SinArcsinh warped BLR, for the female and male cohorts respectively. In images E and F quantile-quantile (QQ) plots of the two models are shown, demonstrating a better fit for the data using a warped BLR model.

349 6771, 'Errors before selecting correct item in alphanumeric path (trail #2)'
350 $W = 8.3105$, $p < 0.001$. The results show an association between the change
351 in cognition and the change in WMH deviance scores.

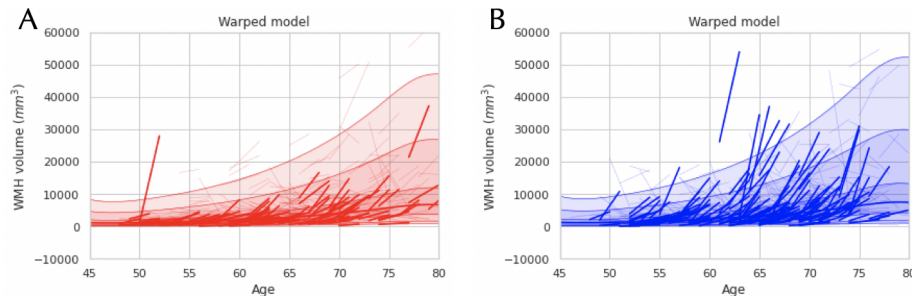


Figure 5: Here the longitudinal follow-up data of the WMHs is plotted for females (A) and males (B), using a SinhArcsinh warped BLR model.

352 3.2. Scalability to a whole brain voxelwise based analysis

353 For the follow-up analysis, we evaluated the warped BLR approach on a
354 whole-brain level for two DTI imaging modalities (FA and MD). The results
355 of these two modalities were very similar and therefore we will only present
356 the results for FA here. We separated the entire dataset into 80% training
357 data and 20% testing data. First, we computed the time complexity per
358 model fit (e.g. for one voxel) with varying number of subjects using the B-
359 spline BLR model setting and compared it to the Gaussian process regression
360 setting (Figure 6). This demonstrates the clear computational advantage of
361 the BLR setting for the whole brain analysis.

362 Afterwards, we tested different model settings for the imaging modalities
363 including a standard BLR, B-spline BLR and a SinhArcsinh warped BLR.
364 Figure 7 shows the comparative results in a Bland-Altman plot for the FA
365 dataset (which were similar for the MD dataset). The figure presents the
366 EV, MSL and the BIC for the B-spline BLR and the warped BLR. These
367 results are consistent with the IDPs in that according to the EV and MSL,
368 the models perform quite similarly for most voxels. Although, we would
369 argue that these measures are not necessarily sensitive for the added benefit
370 of the warping of the likelihood, which will mostly affect the predictions in
371 the outer centiles. For the BIC the results demonstrate that the warped BLR
372 is preferred for certain voxels. The voxels where a warped model is favoured
373 generally showed more non-Gaussian behaviour.

374 Finally, We used a paired-sample t-test, pairing the whole brain results
375 (EV, MSL and BIC) of the different models to estimate the difference be-
376 tween performance measures of the warped and non-warped BLR. For MD

377 the following effect sizes were found: $EV : d = 0.33$, $MSLL : d = 0.003$
378 and $BIC : d = -0.79$. For FA the following effect sizes were found: $EV :$
379 $d = 0.028$, $MSLL : d = 0.017$ and $BIC : d = 0.55$. We can see that the
380 difference between the methods is small. Indicating that the B-spline BLR
381 and the warped BLR model are quite similar in their model fit for MD and
382 FA.

383 3.2.1. Correlation deviance scores DTI and cognitive phenotypes

384 Finally, we correlated the Z-scores of the whole brain warped BLR model
385 for the MD dataset to the cognitive phenotypes. First, we scaled the cognitive
386 data and performed a principal component analysis. We selected the first
387 component, which explained 29% of the variance in the data. Afterwards,
388 we made a summary score of the Z-scores for each participant by looking
389 at the largest deviations, which in the limit should follow an extreme value
390 distribution [32]. We fitted a generalized extreme value distribution to the
391 top 1% of the absolute Z-scores of each subject. Subsequently, we computed
392 a Spearman correlation between the extreme values and the first principal
393 component of the cognitive phenotypes, which gave $\rho = 0.158$, $p < 0.001$.
394 The results demonstrate a clear correlation between the warped deviations
395 from normal development and the cognitive phenotypes. This relationship
396 will be explored further in future studies.

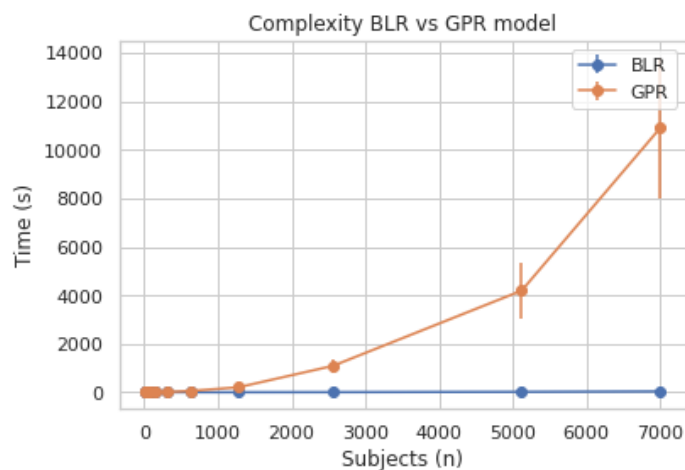


Figure 6: Computational complexity comparison between the Bayesian linear regression (BLR) model setting and the Gaussian process regression (GPR) model setting, giving the mean and the standard error (SE) over ten runs.

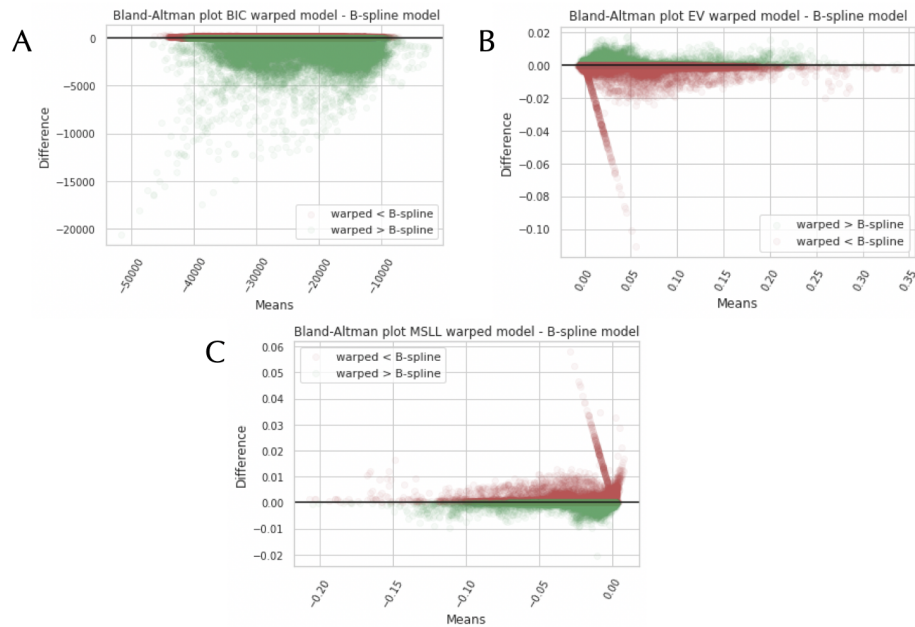


Figure 7: Bland-Altman plots comparing the warped Bayesian Linear Regression (BLR) model to the B-spline BLR model, using Fractional Anisotropy (FA) data. The comparison is done according to the following model selection criteria: The Bayesian Information Criteria (BIC) (A), the Explained Variance (EV) (B), and the Mean Standardized Log Loss (MSLL) (C). The green colour indicates a better fit for the warped BLR.

397 4. Discussion

398 In this paper, we presented a next-generation framework to scale norma-
399 tive models for large population-sized datasets based on warped Bayesian
400 linear regression (BLR). Normative models can capture the heterogeneity
401 in the population and model individual deviations from normal brain de-
402 velopment. We demonstrated that the shift in normative modelling to a
403 B-spline BLR with a likelihood warping gives several benefits. In this study
404 we showed that: (i) Compared to Gaussian process regression, it is compu-
405 tationally much less demanding and is therefore scalable to big datasets. (ii)
406 The non-linearity of the model, incorporated by the B-spline, improves the
407 fit and out of sample predictions for most variables. (iii) Non-Gaussianity
408 of the data can be naturally included due to the incorporation of the likeli-
409 hood warping in the algorithm, which allows for a wider range of datasets to
410 be accurately modelled. (iv) Model selection criteria based on the marginal

411 likelihood, such as the BIC, can be calculated in closed form and therefore
412 a trade-off between model fit and model complexity can be chosen opti-
413 mally from the training data, without cross-validation. (v) The deviations
414 scores from normal brain development can be meaningfully related to be-
415 haviour. Furthermore, we demonstrated the use of the normative model
416 with the warped BLR on different datasets from the UK Biobank, including
417 image-derived phenotypes (IDPs); focusing on white matter hyperintensities
418 (WMHs) as an example of non-Gaussianity and a diffusion tensor imaging
419 (DTI) modality for a whole-brain model.

420 Our proposed method makes it possible to apply normative modelling to
421 considerably larger samples than was feasible before [7], [8]. The results from
422 the computational experiments on the whole brain model showed that the
423 BLR method is scalable to population-sized data sets and fine-grained voxel-
424 level data. In comparison, most normative models used Gaussian process
425 regression, which due to its high computational complexity could only be
426 used in studies with a relatively low sample size. This improvement is mainly
427 because the approximation of the covariance matrix by a set of basis functions
428 allowed us to account for non-linearity in a computationally less demanding
429 way than the Gaussian process regression method, therefore making the B-
430 spline BLR scalable for big datasets. Computationally scalable modelling
431 of nonlinear effects is important since our experiments showed that a cubic
432 B-spline transformation of the age covariate improved model fit compared to
433 linear models for most neuroimaging modalities.

434 Another major benefit of our method is the possibility of modelling non-
435 Gaussian distribution by the use of the likelihood warping technique. This
436 is important in general, as the aim of normative modelling is to accurately
437 model the centiles of variation in addition to modelling the mean and is
438 especially important for normative modelling of variables that are not ap-
439 proximately Gaussian distributed. For example, we showed that the WMHs
440 show non-Gaussian behaviour that is well suited to uncover the benefits of
441 the warped model over the standard model. We demonstrated the improved
442 fit of the WMHs by including a B-spline transformation and a SinhArcsinh
443 likelihood warping in the normative model, which was also exemplified for
444 the longitudinal data. The same improvement in fit for other data modalities
445 that showed more non-Gaussianity in their residuals was also demonstrated
446 by comparing the warped BLR to the B-spline BLR for all the IDPs. Fur-
447 thermore, it was shown on a whole-brain model of a DTI modality that for
448 several voxels the warped BLR gives a better model performance than a

449 B-spline BLR.

450 We emphasize that the addition of non-linear effects and non-gaussianity
451 makes the model more flexible which increase the need for model selection
452 in order to avoid possible overfitting. We presented several model selection
453 criteria that can be used to choose the optimal model settings for different
454 neuroimaging modalities. It should be recognized that for some IDPs and
455 voxels the B-spline BLR gives a better fit, showing that a more flexible
456 model is not always needed. Therefore, we recommend carefully examining
457 the type of data one wants to model and based on the data trends found
458 for the residuals (Gaussian or non-Gaussian) to decide if a more flexible
459 model is preferred. This can easily be checked by looking at the skewness
460 and kurtosis of the distribution or making a QQ-plot. Additionally, different
461 model selection criteria can sometimes contradict each other, as they are
462 sensitive to different parts of the data. As we showed above, classical metrics
463 such as EV and MSLL are not very sensitive to the shape of the predictive
464 distribution. The consequence is that per task, we have to decide if we
465 want a better EV, most sensitive to the mean fit and dependent on the
466 flexibility of the model, or a better MSLL/BIC, which is more sensitive to
467 the variance and penalizes the flexibility of the model. The variability in
468 model selection criteria demonstrates that for different imaging modalities,
469 different normative modelling settings are preferred and the added flexibility
470 is confirmed to only give an advantage for response variables that show non-
471 Gaussianity in their residuals.

472 We confirmed that the deviations from the normative modelling frame-
473 work can be meaningfully related to behaviour. We established a significant
474 correlation between the warped deviance scores from the IDPs and several
475 dimensions of the intelligence phenotype. These tests give a first indication
476 of the possible relationships between the deviations and behaviour. For the
477 whole brain model, the relationship with behaviour was shown with a sig-
478 nificant correlation between an approximation to the g-factor in the form of
479 the first principal component of the cognitive phenotypes and the warped
480 deviance scores. This study demonstrates that the model could be extended
481 to make predictive scores not only in the brain domain, but also for the be-
482 havioural phenotype. In the future, the neurobiological markers of deviation
483 from normal development can be extended to become markers of psychiatric
484 disorders. This has already been done on a smaller scale, using normative
485 modelling [9], [10], [13], [30], [33], [34], but we would like to extend these
486 studies to bigger data models, which include a wide variety of neuroimaging

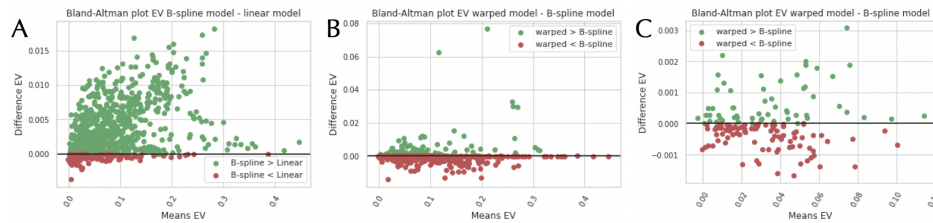


Figure A.8: Bland-Altman plots of the Explained Variance (EV): Figure A shows the comparison of the linear and B-spline model, using the IDPs. Figure B shows the comparison of the warped and B-spline model, using the IDPs. Figure C shows the comparison of the warped and B-spline model, using the FreeSurfer measurements.

487 data modalities.

488 In conclusion, the current study suggests that non-linearity and non-
489 Gaussianity are two parameters of big neuroimaging datasets that need to
490 be captured to make accurate predictions for normal brain development. In
491 this paper, we have done that through a warped BLR normative model.
492 We have shown using several neuroimaging modalities the benefit of this
493 model over more conservative models. Caution is essential when applying
494 non-Gaussian models, as they can overfit and should mainly be used in the
495 presence of non-normally distributed residuals. We recommend carefully
496 assessing the distribution of residuals and the model selection parameters
497 using the different model selection criteria mentioned in this paper that give
498 a balance between model complexity and model fit.

499 Appendix A.

500 Figure A.8 shows the Bland-Altman plots of the explained variance for the
501 IDPs and FreeSurfer measurements comparing the different model settings.

502 Appendix B.

503 An example list of the IDPs, processed using FUNPACK (the FMRIB
504 UKBiobank Normalisation, Parsing And Cleaning Kit), used in this study
505 is given in B.1. The IDPs contained the following neuroimaging modalities
506 [17]:

- 507 1. T1, from which the total brain volumes are calculated.

Table B.1: Example list of the IDP field names, processed using FUNPACK (the FMRIB UKBiobank Normalisation, Parsing And Cleaning Kit).

Volumetric scaling from T1 head image to standard space
Volume of white matter
Median T2star in thalamus (left)
Mean FA in middle cerebellar peduncle on FA skeleton
Mean MD in middle cerebellar peduncle on FA skeleton
Mean MO in fornix on FA skeleton
Mean L1 in body of corpus callosum on FA skeleton
Mean L2 in cerebral peduncle on FA skeleton (right)
Mean L2 in cerebral peduncle on FA skeleton (right)
Mean OD in posterior limb of internal capsule on FA skeleton (right)
Mean ISOVF in splenium of corpus callosum on FA skeleton
Weighted-mean FA in tract acoustic radiation (left)
Weighted-mean MD in tract corticospinal tract (right)
Weighted-mean MO in tract acoustic radiation (right)
Weighted-mean L1 in tract acoustic radiation (left)
Weighted-mean L2 in tract acoustic radiation (left)
Discrepancy between T2 FLAIR brain image and T1 brain image
Volume of grey matter in Frontal Pole (left)

- 508 2. Resting-state fMRI, from which the apparent connectivity between cer-
509 tain brain regions is estimated.
- 510 3. Task fMRI, from which the strength of response to certain tasks is
511 given, which can be related to higher cognitive functioning.
- 512 4. T2 Flair, from which the white matter lesions are estimated.
- 513 5. DMRI, from which the DTI measures such as FA and MD are calcu-
514 lated.
- 515 6. Susceptibility-weighted imaging (SWI), from which venous vasculature,
516 microbleed and other aspects of microstructure are estimated.

517 Appendix C.

518 We computed the differences between the BICs of a B-spline BLR and
519 a warped BLR. Afterwards, we selected the top 30 IDPs where the B-spline
520 model had the lowest BIC comparatively to the warped score or the other

521 way around. In table C.2 the model selection criteria of the top 30 best-fitted
522 IDPs with the B-spline BLR compared to the warped BLR are shown. In
523 table C.3 the model selection criteria of the top 30 best-fitted IDPs with the
524 warped BLR compared to the B-spline BLR shown. These tables demon-
525 strate that every neuroimaging modality has its optimal model settings and
526 that one should carefully examine the model selection criteria and shape of
527 the response distribution, before choosing a model.

528 **Appendix D.**

529 We used a paired-sample t-test, pairing the IDP results (EV, MSLI and
530 BIC) of the different models to estimate the difference between performance
531 measures of the warped and non-warped BLR. In table D.4 and D.5 the
532 Cohen’s d effect sizes and p-values are reported. The results show that there
533 is a large difference between the standard BLR and the B-spline BLR, which
534 confirms that one should take into account the non-linearity of the data.
535 For the warped BLR and the B-spline BLR model, there is only a significant
536 difference in the BIC score. We argue that this is because the model selection
537 criteria are not necessarily sensitive to the deviations in the residuals from
538 normality. Therefore, we also recommend to, alongside the model selection
539 criteria, look at the skewness and kurtosis values together with the QQ-plot
540 to choose the optimal model settings for each modality.

541 **Appendix E.**

542 In table E.6 we listed the cognitive variables from the UK Biobank that
543 were used in this study with their IDs.

544 **References**

- 545 [1] C. Sudlow, J. Gallacher, N. Allen, V. Beral, P. Burton, J. Danesh,
546 P. Downey, P. Elliott, J. Green, M. Landray, et al., Uk biobank: an
547 open access resource for identifying the causes of a wide range of com-
548 plex diseases of middle and old age, *Plos med* 12 (2015) e1001779.
549 doi:10.1371/journal.pmed.1001779.
- 550 [2] P. M. Thompson, J. L. Stein, S. E. Medland, D. P. Hibar, A. A. Vasquez,
551 M. E. Renteria, R. Toro, N. Jahanshad, G. Schumann, B. Franke, et al.,

EV	MSLL	BIC	Field
0.206	-0.115	-166562.002	Mean MD in superior fronto-occipital fasciculus on FA skeleton (right)
0.134	-0.072	-46220.575	Mean ISOVF in genu of corpus callosum on FA skeleton
0.025	-0.013	-12455.567	Mean MO in superior fronto-occipital fasciculus on FA skeleton (left)
0.159	-0.087	-163761.463	Mean L2 in superior fronto-occipital fasciculus on FA skeleton (right)
0.148	-0.08	-176269.475	Mean MD in external capsule on FA skeleton (right)
0.17	-0.093	-40955.602	Discrepancy between T1 brain image and standard-space brain template (linearly-aligned)
0.074	-0.039	-52218.319	Mean ISOVF in anterior limb of internal capsule on FA skeleton (left)
0.066	-0.034	-50151.283	Mean ISOVF in anterior limb of internal capsule on FA skeleton (right)
0.135	-0.072	-175704.326	Mean L3 in external capsule on FA skeleton (right)
0.202	-0.113	-32491.645	Mean ICVF in superior fronto-occipital fasciculus on FA skeleton (right)
0.077	-0.04	-99708.396	Inverted temporal signal-to-noise ratio in pre-processed tfMRI
0.188	-0.104	-171678.769	Mean MD in anterior corona radiata on FA skeleton (left)
0.265	-0.154	-176057.846	Weighted-mean MD in tract anterior thalamic radiation (left)
0.078	-0.041	-44211.387	Mean ISOVF in superior fronto-occipital fasciculus on FA skeleton (left)
0.143	-0.077	-59646.162	Weighted-mean ISOVF in tract anterior thalamic radiation (right)
0.177	-0.098	-172620.769	Mean MD in anterior corona radiata on FA skeleton (right)
0.273	-0.16	-176331.153	Weighted-mean MD in tract anterior thalamic radiation (right)
0.174	-0.096	-170432.707	Mean L2 in anterior corona radiata on FA skeleton (right)
0.054	-0.028	101219.506	Volume of grey matter in Pallidum (right)
0.175	-0.096	-169471.163	Mean MD in genu of corpus callosum on FA skeleton
0.229	-0.13	-175866.701	Weighted-mean L2 in tract anterior thalamic radiation (right)
0.163	-0.089	-177074.476	Mean MD in anterior limb of internal capsule on FA skeleton (left)
0.079	-0.041	-53234.386	Mean ISOVF in posterior corona radiata on FA skeleton (left)
0.159	-0.087	-58912.836	Weighted-mean ISOVF in tract anterior thalamic radiation (left)
0.04	-0.02	-25966.018	Mean ICVF in fornix on FA skeleton
0.076	-0.04	-56374.466	Mean ISOVF in anterior corona radiata on FA skeleton (left)
0.14	-0.075	-55319.609	Weighted-mean OD in tract superior thalamic radiation (left)
0.076	-0.039	-57122.197	Weighted-mean ISOVF in tract superior longitudinal fasciculus (left)
0.039	-0.02	-57205.686	Mean ISOVF in anterior corona radiata on FA skeleton (right)
0.103	-0.054	-51036.79	Mean ISOVF in posterior corona radiata on FA skeleton (right)

Table C.2: Model selection criteria of the top 30 IDPs, ranked according to difference between the BIC of a B-spline BLR and a SinhArcsinh warped BLR, where the B-spline BLR had a lower BIC score.

EV	MSLL	BIC	Field
0.249	-0.143	184900.524	Total volume of white matter hyperintensities (from T1 and T2-FLAIR images)
0.147	-0.079	-29710.013	Mean OD in fornix on FA skeleton
0.285	-0.164	-137192.133	Mean MD in fornix on FA skeleton
0.276	-0.153	-136161.29	Mean L3 in fornix on FA skeleton
0.275	-0.151	-134595.545	Mean L2 in fornix on FA skeleton
0.153	-0.083	-87376.141	Inverted temporal signal-to-noise ratio in pre-processed rfMRI
0.27	-0.157	-24636.152	Mean FA in fornix on FA skeleton
0.171	-0.093	-32985.173	Mean MO in anterior limb of internal capsule on FA skeleton (right)
0.094	-0.049	-22330.216	Mean MO in tapetum on FA skeleton (left)
0.043	-0.022	-26681.768	Mean MO in tapetum on FA skeleton (right)
0.141	-0.076	-33305.028	Mean MO in anterior limb of internal capsule on FA skeleton (left)
0.054	-0.027	-42459.737	Weighted-mean ISOVF in tract parahippocampal part of cingulum (left)
0.117	-0.062	-71451.215	Mean OD in splenium of corpus callosum on FA skeleton
0.064	-0.033	-40476.534	Weighted-mean FA in tract parahippocampal part of cingulum (right)
0.307	-0.183	-15506.712	Mean ISOVF in fornix on FA skeleton
0.182	-0.1	-34039.973	Discrepancy between T2 FLAIR brain image and T1 brain image
0.047	-0.024	-41660.315	Weighted-mean FA in tract parahippocampal part of cingulum (left)
0.058	-0.03	-51125.932	Mean OD in tapetum on FA skeleton (left)
0.199	-0.111	-172072.977	Weighted-mean MD in tract posterior thalamic radiation (left)
0.311	-0.186	-26746.982	Discrepancy between tfMRI brain image and T1 brain image
0.131	-0.071	-169248.259	Mean MD in posterior thalamic radiation on FA skeleton (left)
0.089	-0.046	-181090.417	Mean MD in inferior cerebellar peduncle on FA skeleton (left)
0.07	-0.036	-41654.584	Weighted-mean ISOVF in tract parahippocampal part of cingulum (right)
0.028	-0.014	-35788.551	Mean MO in posterior limb of internal capsule on FA skeleton (right)
0.069	-0.036	-62423.772	Weighted-mean OD in tract forceps major
0.027	-0.014	-52538.461	Mean ISOVF in middle cerebellar peduncle on FA skeleton
0.314	-0.188	-27837.003	Discrepancy between rfMRI brain image and T1 brain image
0.085	-0.044	-170720.346	Weighted-mean MD in tract medial lemniscus (right)

Table C.3: Model selection criteria of the top 30 IDPs, ranked according to the difference between the BIC of a B-spline BLR and a SinhArcsinh warped BLR, where the SinhArcsinh warped BLR had a lower BIC score.

- 552 The enigma consortium: large-scale collaborative analyses of neuroimag-
 553 ing and genetic data, *Brain imaging and behavior* 8 (2014) 153–182.
 554 doi:10.1007/s11682-013-9269-5.
- 555 [3] B. Casey, T. Cannonier, M. I. Conley, A. O. Cohen, D. M. Barch, M. M.
 556 Heitzeg, M. E. Soules, T. Teslovich, D. V. Dellarco, H. Garavan, et al.,
 557 The adolescent brain cognitive development (abcd) study: imaging ac-
 558 quisition across 21 sites, *Developmental cognitive neuroscience* 32 (2018)
 559 43–54. doi:10.1016/j.dcn.2018.03.001.
- 560 [4] T. D. Satterthwaite, J. J. Connolly, K. Ruparel, M. E. Calkins, C. Jack-
 561 son, M. A. Elliott, D. R. Roalf, R. Hopson, K. Prabhakaran, M. Behr,
 562 et al., The philadelphia neurodevelopmental cohort: A publicly avail-
 563 able resource for the study of normal and abnormal brain development in
 564 youth, *Neuroimage* 124 (2016) 1115–1119. doi:10.1016/j.neuroimage.
 565 2015.03.056.
- 566 [5] T. R. Insel, B. N. Cuthbert, Brain disorders? Precisely: Precision
 567 medicine comes to psychiatry, *Science* 348 (2015) 499–500. doi:10.1126/
 568 science.aab2358.

Criteria	t	p	d
EV	27.511	$p < 0.001$	0.922
MSLL	-26.538	$p < 0.001$	-0.889
BIC	-15.95	$p < 0.001$	-0.534

Table D.4: Table presenting a paired-sample t-test between the B-spline and standard BLR models, using the IDP data, showing a significant difference between the model selection criteria of the B-spline BLR and the standard BLR, with a large effect size.

Criteria	t	p	d
EV	-0.897	0.37	-0.03
MSLL	0.026	0.979	0.001
BIC	9.279	$p < 0.001$	0.311

Table D.5: Table presenting a paired-sample t-test between the B-spline and warped BLR models, using the IDP data, showing only a significant difference between the model selection criteria of the B-spline BLR and the B-spline SinhArcsinh warped BLR using the BIC score, with a small effect size.

Table E.6: Cognitive variables of the UK Biobank that were used in this study.

Field	FieldID
Number of times snap-button pressed	403
Duration to first press of snap-button in each round	404
Mean time to correctly identify matches	20023
Time elapsed	4256
Digits entered correctly	4259
Number of rounds of numeric memory test performed	4283
Time to complete test	4285
Duration screen displayed	4290
Number of attempts	4291
Prospective memory result	20018
Fluid intelligence score	20016
Number of fluid intelligence questions attempted within time limit	20128
Duration to complete numeric path (trail 1)	6348
Total errors traversing numeric path (trail 1)	6349
Duration to complete alphanumeric path (trail 2)	6350
Total errors traversing alphanumeric path (trail 2)	6351
Errors before selecting correct item in numeric path (trail 1)	6770
Errors before selecting correct item in alphanumeric path (trail 2)	6771
Interval between previous point and current one in numeric path (trail 1)	6772
Interval between previous point and current one in alphanumeric path (trail 2)	6773
Number of puzzles correctly solved	6373
Number of puzzles viewed	6374
Number of puzzles correct	6382
Number of puzzles attempted	6383
Number of puzzles correct	21004
Number of symbol digit matches attempted	23323
Number of symbol digit matches made correctly	23324

- 569 [6] T. Wolfers, J. K. Buitelaar, C. F. Beckmann, B. Franke, A. F. Mar-
570 quand, From estimating activation locality to predicting disorder: A
571 review of pattern recognition for neuroimaging-based psychiatric diag-
572 nostics, 2015. doi:10.1016/j.neubiorev.2015.08.001.
- 573 [7] A. F. Marquand, S. M. Kia, M. Zabihi, T. Wolfers, J. K. Buitelaar,
574 C. F. Beckmann, Conceptualizing mental disorders as deviations from
575 normative functioning, 2019. doi:10.1038/s41380-019-0441-1.
- 576 [8] A. F. Marquand, I. Rezek, J. Buitelaar, C. F. Beckmann, Understanding
577 Heterogeneity in Clinical Cohorts Using Normative Models: Beyond
578 Case-Control Studies, *Biological Psychiatry* 80 (2016a) 552–561. doi:10.
579 1016/j.biopsych.2015.12.023.
- 580 [9] T. Wolfers, N. T. Doan, T. Kaufmann, D. Alnæs, T. Moberget,
581 I. Agartz, J. K. Buitelaar, T. Ueland, I. Melle, B. Franke, O. A. An-
582 dreassen, C. F. Beckmann, L. T. Westlye, A. F. Marquand, Map-
583 ping the Heterogeneous Phenotype of Schizophrenia and Bipolar Disor-
584 der Using Normative Models, *JAMA Psychiatry* 75 (2018) 1146–1155.
585 doi:10.1001/jamapsychiatry.2018.2467.
- 586 [10] M. Zabihi, M. Oldehinkel, T. Wolfers, V. Frouin, D. Goyard, E. Loth,
587 T. Charman, J. Tillmann, T. Banaschewski, G. Dumas, R. Holt,
588 S. Baron-Cohen, S. Durston, S. Bölte, D. Murphy, C. Ecker, J. K. Buite-
589 laar, C. F. Beckmann, A. F. Marquand, Dissecting the Heterogeneous
590 Cortical Anatomy of Autism Spectrum Disorder Using Normative Mod-
591 els, *Biological Psychiatry: Cognitive Neuroscience and Neuroimaging* 4
592 (2019) 567–578. doi:10.1016/j.bpsc.2018.11.013.
- 593 [11] T. Kaufmann, D. van der Meer, N. T. Doan, E. Schwarz, M. J. Lund,
594 I. Agartz, D. Alnæs, D. M. Barch, R. Baur-Streubel, A. Bertolino,
595 F. Bettella, M. K. Beyer, E. Bøen, S. Borgwardt, C. L. Brandt, J. Buite-
596 laar, E. G. Celius, S. Cervenka, A. Conzelmann, A. Córdova-Palomera,
597 A. M. Dale, D. J. de Quervain, P. D. Carlo, S. Djurovic, E. S. Dørum,
598 S. Eisenacher, T. Elvsåshagen, T. Espeseth, H. Fatouros-Bergman,
599 L. Flyckt, B. Franke, O. Frei, B. Haatveit, A. K. Håberg, H. F. Harbo,
600 C. A. Hartman, D. Heslenfeld, P. J. Hoekstra, E. A. Høgestøl, T. L.
601 Jernigan, R. Jonassen, E. G. Jönsson, L. Farde, L. Flyckt, G. En-
602 gberg, S. Erhardt, H. Fatouros-Bergman, S. Cervenka, L. Schwieler,

- 603 F. Piehl, I. Agartz, K. Collste, P. Victorsson, A. Malmqvist, M. Hedberg,
604 F. Orhan, P. Kirsch, I. Kłoszewska, K. K. Kolskår, N. I. Landrø, S. L.
605 Hellard, K. P. Lesch, S. Lovestone, A. Lundervold, A. J. Lundervold,
606 L. A. Maglanoc, U. F. Malt, P. Mecocci, I. Melle, A. Meyer-Lindenberg,
607 T. Moberget, L. B. Norbom, J. E. Nordvik, L. Nyberg, J. Oosterlaan,
608 M. Papalino, A. Papassotiropoulos, P. Pauli, G. Pergola, K. Persson,
609 G. Richard, J. Rokicki, A. M. Sanders, G. Selbæk, A. A. Shadrin, O. B.
610 Smeland, H. Soininen, P. Sowa, V. M. Steen, M. Tsolaki, K. M. Ul-
611 richsen, B. Vellas, L. Wang, E. Westman, G. C. Ziegler, M. Zink, O. A.
612 Andreassen, L. T. Westlye, Common brain disorders are associated with
613 heritable patterns of apparent aging of the brain, *Nature Neuroscience*
614 22 (2019) 1617–1623. doi:10.1038/s41593-019-0471-7.
- 615 [12] A. F. Marquand, T. Wolfers, M. Mennes, J. Buitelaar, C. F. Beck-
616 mann, Beyond Lumping and Splitting: A Review of Computational
617 Approaches for Stratifying Psychiatric Disorders, 2016b. doi:10.1016/
618 j.bpsc.2016.04.002.
- 619 [13] J. Lv, M. Di Biase, R. F. Cash, L. Cocchi, V. Croypley, P. Klauser,
620 Y. Tian, J. Bayer, L. Schmaal, S. Cetin-Karayumak, et al., Individ-
621 ual deviations from normative models of brain structure in a large
622 cross-sectional schizophrenia cohort, *bioRxiv* (2020). doi:10.1038/
623 s41380-020-00882-5.
- 624 [14] S. M. Kia, A. Marquand, Normative Modeling of Neuroimaging Data us-
625 ing Scalable Multi-Task Gaussian Processes, *Lecture Notes in Computer*
626 *Science (including subseries Lecture Notes in Artificial Intelligence and*
627 *Lecture Notes in Bioinformatics)* 11072 LNCS (2018) 127–135. URL:
628 <http://arxiv.org/abs/1806.01047>. arXiv:1806.01047.
- 629 [15] C. E. Rasmussen, C. K. Williams, *Approximation methods for large*
630 *datasets* (2005).
- 631 [16] I. Huertas, M. Oldehinkel, E. S. van Oort, D. Garcia-Solis, P. Mir, C. F.
632 Beckmann, A. F. Marquand, A Bayesian spatial model for neuroimaging
633 data based on biologically informed basis functions, *NeuroImage* 161
634 (2017) 134–148. doi:10.1016/j.neuroimage.2017.08.009.
- 635 [17] F. Alfaro-Almagro, M. Jenkinson, N. K. Bangerter, J. L. Andersson,
636 L. Griffanti, G. Douaud, S. N. Sotiropoulos, S. Jbabdi, M. Hernandez-

- 637 Fernandez, E. Vallee, et al., Image processing and quality control for
638 the first 10,000 brain imaging datasets from uk biobank, *Neuroimage*
639 166 (2018) 400–424. doi:10.1016/j.neuroimage.2017.10.034.
- 640 [18] M. Habes, R. Pomponio, H. Shou, J. Doshi, E. Mamourian, G. Erus,
641 I. Nasrallah, L. J. Launer, T. Rashid, M. Bilgel, et al., The brain chart
642 of aging: Machine-learning analytics reveals links between brain aging,
643 white matter disease, amyloid burden, and cognition in the istaging
644 consortium of 10,216 harmonized mr scans, *Alzheimer’s & Dementia*
645 (2020). doi:10.1002/alz.12178.
- 646 [19] S. R. Cox, S. J. Ritchie, E. M. Tucker-Drob, D. C. Liewald, S. P.
647 Hagenaaars, G. Davies, J. M. Wardlaw, C. R. Gale, M. E. Bastin,
648 I. J. Deary, Ageing and brain white matter structure in 3,513 uk
649 biobank participants, *Nature communications* 7 (2016) 1–13. doi:10.
650 1038/ncomms13629.
- 651 [20] K. L. Miller, F. Alfaro-Almagro, N. K. Bangerter, D. L. Thomas, E. Ya-
652 coub, J. Xu, A. J. Bartsch, S. Jbabdi, S. N. Sotiropoulos, J. L. An-
653 dersson, L. Griffanti, G. Douaud, T. W. Okell, P. Weale, I. Dragonu,
654 S. Garratt, S. Hudson, R. Collins, M. Jenkinson, P. M. Matthews,
655 S. M. Smith, Multimodal population brain imaging in the UK Biobank
656 prospective epidemiological study, *Nature Neuroscience* 19 (2016) 1523–
657 1536. doi:10.1038/nn.4393.
- 658 [21] P. McCarthy, funpack, 2020. doi:10.5281/zenodo.3761702.
- 659 [22] C. Fawns-Ritchie, I. J. Deary, Reliability and validity of the UK Biobank
660 cognitive tests, *PLoS ONE* 15 (2020). doi:10.1371/journal.pone.
661 0231627.
- 662 [23] D. M. Lyall, B. Cullen, M. Allerhand, D. J. Smith, D. Mackay, J. Evans,
663 J. Anderson, C. Fawns-Ritchie, A. M. McIntosh, I. J. Deary, J. P. Pell,
664 Cognitive Test Scores in UK Biobank: Data Reduction in 480,416 Par-
665 ticipants and Longitudinal Stability in 20,346 Participants, *PLOS ONE*
666 11 (2016) e0154222. URL: <https://dx.plos.org/10.1371/journal.pone.0154222>. doi:10.1371/journal.pone.0154222.
- 668 [24] A. M. Fjell, K. B. Walhovd, L. T. Westlye, Y. Østby, C. K. Tamnes, T. L.
669 Jernigan, A. Gamst, A. M. Dale, When does brain aging accelerate?

- 670 dangers of quadratic fits in cross-sectional studies, *Neuroimage* 50 (2010)
671 1376–1383. doi:10.1016/j.neuroimage.2010.01.061.
- 672 [25] S. M. Kia, H. Huijsdens, R. Dinga, T. Wolfers, M. Mennes, O. A. An-
673 dreassen, L. T. Westlye, C. F. Beckmann, A. F. Marquand, Hierarchical
674 bayesian regression for multi-site normative modeling of neuroimaging
675 data, arXiv preprint arXiv:2005.12055 (2020).
- 676 [26] C. M. Bishop, *Pattern recognition and machine learning*, springer, 2006.
- 677 [27] E. Snelson, Z. Ghahramani, C. E. Rasmussen, Warped gaussian pro-
678 cesses, in: *Advances in neural information processing systems*, 2004,
679 pp. 337–344.
- 680 [28] G. Rios, F. Tobar, Compositionally-warped gaussian processes, *Neural*
681 *Networks* 118 (2019) 235–246. doi:10.1016/j.neunet.2019.06.012.
- 682 [29] M. C. Jones, A. Pewsey, Sinh-arcsinh distributions, *Biometrika* 96
683 (2009) 761–780. doi:10.1093/biomet/asp053.
- 684 [30] A. F. Marquand, I. Rezek, J. Buitelaar, C. F. Beckmann, Understanding
685 heterogeneity in clinical cohorts using normative models: beyond case-
686 control studies, *Biological psychiatry* 80 (2016) 552–561. doi:10.1016/
687 j.biopsych.2015.12.023.
- 688 [31] G. Nave, W. H. Jung, R. Karlsson Linnér, J. W. Kable, P. D. Koellinger,
689 Are Bigger Brains Smarter? Evidence From a Large-Scale Prereg-
690 istered Study, *Psychological Science* 30 (2019) 43–54. URL: <http://journals.sagepub.com/doi/10.1177/0956797618808470>. doi:10.
691 1177/0956797618808470.
- 692
- 693 [32] R. A. Fisher, L. H. C. Tippett, Limiting forms of the frequency distri-
694 bution of the largest or smallest member of a sample, in: *Mathematical*
695 *Proceedings of the Cambridge Philosophical Society*, volume 24, Cam-
696 bridge University Press, 1928, pp. 180–190.
- 697 [33] T. Wolfers, C. F. Beckmann, M. Hoogman, J. K. Buitelaar, B. Franke,
698 A. F. Marquand, Individual differences v. the average patient: Map-
699 ping the heterogeneity in ADHD using normative models, *Psychologi-*
700 *cal Medicine* 50 (2019) 314–323. URL: <https://pubmed.ncbi.nlm.nih.gov/30782224/>. doi:10.1017/S0033291719000084.
701

- 702 [34] M. Zabihi, D. L. Floris, S. M. Kia, T. Wolfers, J. Tillmann, A. L. Are-
703 nas, C. Moessnang, T. Banaschewski, R. Holt, S. Baron-Cohen, E. Loth,
704 T. Charman, T. Bourgeron, D. Murphy, C. Ecker, J. K. Buitelaar,
705 C. F. Beckmann, A. Marquand, Fractionating autism based on neu-
706 roanatomical normative modeling, *Translational Psychiatry* 10 (2020)
707 1–10. doi:10.1038/s41398-020-01057-0.